# Consistent perturbative modeling of pseudo-Newtonian core-collapse supernova simulations

John Ryan Westernacher-Schneider<sup>®</sup>

Department of Astronomy/Steward Observatory, The University of Arizona, 933 North Cherry Avenue, Tucson, Arizona 85721, USA

(Received 18 February 2020; accepted 6 April 2020; published 16 April 2020)

We write down and apply the linearized fluid and gravitational equations consistent with pseudo-Newtonian simulations, whereby Newtonian hydrodynamics is used with a pseudo-Newtonian monopole and standard Newtonian gravity for higher multipoles. We thereby eliminate the need to use mode function matching to identify the active nonradial modes in pseudo-Newtonian core-collapse supernova simulations, in favor of the less complex and less costly mode frequency matching method. In doing so, we are able to measure appropriate boundary conditions for a mode calculation.

DOI: 10.1103/PhysRevD.101.083021

#### I. INTRODUCTION

There is increasing attention to gravitational wave asteroseismology of core-collapse supernovae (CCSNe) from a theoretical perspective (e.g., Refs. [1–13]). One challenge is identifying which hydrodynamical modes of the system are producing gravitational wave (GW) emission in simulations. This requires modeling in postprocess. One strategy is to use simulation snapshots as background solutions for a perturbative mode calculation. Once the perturbative mode spectrum is obtained, a matching procedure is necessary to determine which modes are actually active in the simulation. A mode frequency matching procedure has been used frequently [5–7], whereby the evolution of perturbative mode frequencies are overlaid on simulation gravitational wave spectrograms, and then matching is judged by frequency coincidence over time.

However, some mode classes (particularly p-modes) tend to have frequencies which are roughly constant multiples of each other over time, with neighboring modes having frequencies being roughly between 5% to 10% away. Frequency mismatches between simulations and perturbative calculations can arise due to the use of different equations of motion in the simulations vs those used in the perturbative calculation. For example, in Refs. [5,7], the general relativistic hydrodynamic equations were used in the perturbative calculation, with either no metric perturbations [5] or a subset of possible metric perturbations [7]. Their simulations correspondingly use general relativistic hydrodynamics and a spatially conformally flat metric approximation for spacetime. As another example, Ref. [6] uses for its perturbative equations general relativistic hydrodynamics with either no metric perturbations or only lapse perturbations,

supplemented with a Poisson equation to solve for the lapse perturbation. Their simulations, on the other hand, use Newtonian hydrodynamics and pseudo-Newtonian gravity. The ensuing frequency mismatches generated by the use of different equations may result in mode misidentification during a mode frequency matching procedure, particularly due the absence of the lapse function in the hydrodynamic fluxes in the simulations.

In Refs. [8,12], a mode function matching procedure was followed instead. This entails comparing the mode functions computed perturbatively with the velocity data in the simulation. As in Ref. [6], the simulations were pseudo-Newtonian, whereas the perturbative calculation used the general relativistic hydrodynamic equations in the Cowling approximation (no metric perturbations), with the lapse function being the only nonzero metric component. The mode function matching procedure produced convincing mode identification despite the use of perturbative equations that are not consistent with the simulation, because neighboring mode functions have distinct enough morphology that the best-fitting mode function is clearly superior to the next-best-fitting one (provided the mode's excitation is large enough with respect to stochastic or nonlinear motions). A frequency mismatch between the best-fitting mode functions and the simulation frequencies of order  $\sim$ 15% was observed in Refs. [8,12] and is large enough to have caused a mode misidentification via mode frequency matching. During targeted modeling of the next galactic core-collapse supernova, this would have produced incorrect inferences about the source. Furthermore, mode misidentification in simulations can misinform analytic or semianalytic modeling efforts of these systems.

However, mode function matching is considerably more complex and expensive than mode frequency matching. It is more complex because frequency masks have to be

<sup>\*</sup>iwestern@email.arizona.edu

determined in order to apply appropriate spectral filtering on the velocity data from the simulation. It is more expensive because the entire fluid data in the system must be saved with sufficient temporal cadence such that the spectral resolution allows a clean Fourier extraction of individual mode activity. In Refs. [8,12], axisymmetric simulations were performed, which alleviated the storage issue, but one wishes to identify modes in fully three-dimensional simulations as well. Large searches of the CCSN progenitor parameter space would be hampered by the need to perform mode function matching. It would therefore be desirable to use the perturbative equations that are consistent with simulations, which remove the need for the expensive mode function matching procedure.

In this work, we write down and apply the consistent linearized equations appropriate for pseudo-Newtonian codes such as PROMETHEUS/VERTEX [2,14-17], FLASH [18,19], FORNAX [20], and CHIMERA [21]. As long as one does not solve for radial modes, these equations are simply the standard Newtonian ones. During testing, we identify and correct a mistreatment of the boundary conditions [6,8,12] for the gravitational potential perturbation. We are able to reproduce the quadrupolar mode frequencies of an equilibrium star evolved using FLASH. When applied to a CCSN simulation, we find the best-fitting mode functions have the correct frequency (i.e., agreeing with the simulation) at the 2% or sub-1% level, depending on the boundary conditions used. We also perform a residual test with the spherically symmetric Euler equation, showing that the state of hydrostatic equilibrium (assumed in the perturbative calculation) is satisfied only at the  $\sim$ 5% level, whereas the terms coming from a time-dependent or nonsteady  $(v \neq 0)$  background solution are negligible. This serves as a cautionary note for future applications of this perturbative modeling but also suggests that including a time-dependent or nonsteady background would not affect the calculation significantly. We find that the outer boundary condition on the fluid variables yielding the most precise matching with simulations (sub-1% level) is that of Ref. [5], in which the radial displacement is taken to vanish at the shockwave location. The agreement is so striking that we are tempted to conclude that this is the physically correct boundary condition in the early postbounce regime we are considering.

Note that the consistent perturbative modeling of pseudo-Newtonian simulations that we present here does *not* answer the question of whether such simulations yield the correct mode excitation. Previously, in Refs. [8,12], it was shown that *if* the perturbative modeling does not use the linearization of the equations being simulated then mode function matching is necessary to correctly identify the active modes in a simulation. In this work, we simply use the consistent linearization to show that correct identification of active modes in a simulation is possible with mode frequency matching alone, and interesting

physics can then be extracted (such as the physically correct boundary conditions for the perturbations). The question of whether the mode excitation itself is correct in pseudo-Newtonian simulations is left for future work. Previous studies indicate that mode frequencies are systematically shifted with respect to general relativity (see, e.g., Ref. [22]), and overestimated in particular [8,12,22], but one cannot know for sure without directly identifying the excited modes in each case (e.g., by mode function matching). The pitfalls found in Refs. [8,12] in using pseudo-Newtonian simulations to study mode frequencies were anticipated clearly in Ref. [22].

We give a brief summary of the results of Refs. [8,12] in Sec. II. We described our methods in Secs. III and Appendix A and discuss our results in Sec. IV. Tests are presented in Appendix B. We use geometric units G = c = 1 throughout, unless units appear explicitly.

## II. SIMULATIONS AND BACKGROUND INFORMATION

We analyze the nonrotating  $20 M_{\odot}$  zero-age main sequence mass CCSN progenitor presented previously in Refs. [8,12]. It was simulated in axisymmetry using FLASH [18,19] until ~100 ms postbounce. Mild excitations of hydrodynamic modes occur at bounce, the amplitude of which is expected to be artificially enhanced due to asymmetries introduced during collapse by the cylindrical computational grid. However, the strength of excitation does not concern us here—we simply seek to demonstrate mode identification. We defer to Ref. [12] for a more detailed description of the simulation details. We also defer details regarding the mode function matching method to Ref. [8], in which they are described in the most depth. The method involves using spectrogram filter kernels to extract mode motions from the velocity data in the simulations, followed by vector spherical harmonic decompositions to extract the angular harmonic components. The resulting fields are then normalized before their overlaps with perturbative mode functions are computed.

Our main purpose here is to apply a consistent linear perturbative scheme to a snapshot from the simulation at  $t \sim 40$  ms postbounce, which was previously analyzed [8,12], to study multiple quadrupolar modes (l = 2, m = 0) of the system which are excited weakly at bounce. The first mode has a peak frequency of 515 Hz. This mode was found in Refs. [8,12] to have a radial order n = 4, and we make the same conclusion here. The second quadrupolar mode we study has a less well-defined peak frequency (we estimate 1241 Hz from the GW spectrum) and was not reported in Refs. [8,12]. Note that, due to an

<sup>&</sup>lt;sup>1</sup>Note that the mode is described in Ref. [12] as having a frequency of 483 Hz, which is the middle value of the spectrogram filter kernel used to extract it. However, 515 Hz is the location of the peak Fourier amplitude in the GW signal.

analysis error, perturbative mode frequencies in Ref. [8] should be corrected by multiplying them by  $\sim$ 1.5.

#### III. PERTURBATIVE SCHEME

We begin with the Newtonian perfect fluid and gravity equations,

$$\partial_t \rho + \nabla_i (\rho v^i) = 0 \tag{3.1}$$

$$\partial_t(\rho v_i) + \nabla_i(\rho v^j v_i) + \partial_i P = -\rho \partial_i \Phi \qquad (3.2)$$

$$\nabla^2 \Phi = 4\pi \rho. \tag{3.3}$$

We linearize these equations with respect to a spherically symmetric equilibrium background solution,  $\rho = \rho(r)$ ,  $v^i(r) = (v^r(r), 0, 0), \quad P = P(r), \quad \Phi = \Phi(r), \quad \partial_r P/\rho = -\partial_r \Phi.$  Denote Eulerian perturbations with  $\delta$  and Lagrangian ones with  $\Delta$ , and substitute, e.g.,  $\rho \to \rho + \delta \rho$  into Eqs. (3.1)–(3.3). Also, use the condition of adiabatic perturbations coming from the energy equation,

$$\frac{\Delta P}{\Delta \rho} = c_s^2,\tag{3.4}$$

where  $c_s^2 = P\Gamma_1/\rho$  is the sound speed squared,  $\Gamma_1$  is the adiabatic index for the perturbations, and, e.g.,  $\Delta P = \delta P + \xi^i \nabla_i P$ , where  $\xi^i$  is the perturbative Eulerian fluid element displacement vector. The displacement vector  $\xi^i$  is related to the velocity perturbation via  $\delta v^i = \partial_t \xi^i + v^j \nabla_j \xi^i - \xi^j \nabla_j v^i$ , which simplifies to  $\delta v^i = \partial_t \xi^i$  when the background velocity is zero.

Linearization of Eqs. (3.1)–(3.3) assuming axisymmetric perturbations  $\xi^i = (\xi^r, \xi^\theta, 0)$  yields

$$0 = \delta \rho + \rho \xi^i \partial_i \ln \sqrt{\gamma} + \rho \partial_i \xi^i + \xi^r \partial_r \rho \tag{3.5}$$

$$0 = \partial_t^2 \xi^r + \frac{1}{\rho} \partial_r \delta P + \partial_r \delta \Phi - \frac{\delta \rho}{\rho^2} \partial_r P \qquad (3.6)$$

$$0 = r^2 \partial_t^2 \xi^\theta + \frac{1}{\rho} \partial_\theta \delta P + \partial_\theta \delta \Phi \tag{3.7}$$

$$0 = \nabla^2 \delta \Phi - 4\pi \delta \rho, \tag{3.8}$$

where  $\sqrt{\gamma}=r^2\sin\theta$  is the square root of the flat 3-metric determinant in spherical coordinates. In deriving Eq. (3.5), we integrated in time, setting the integration constant to zero [23]. In Eq. (3.7), note the appearance of the factor  $r^2$  in front of the time derivative, which comes from raising the index using the metric via  $\partial_t^2 \xi_\theta = \gamma_{i\theta} \partial_t^2 \xi^i = \gamma_{\theta\theta} \partial_t^2 \xi^\theta = r^2 \partial_t^2 \xi^\theta$ . Using the axisymmetric spherical harmonics  $Y_l$  (m=0) and harmonic time dependence, we insert a separation of variables Ansatz,

$$\begin{split} \delta \rho &= \delta \hat{\rho}(r) Y_l e^{-i\sigma t} \\ \delta P &= \delta \hat{P}(r) Y_l e^{-i\sigma t} \\ \delta \Phi &= \delta \hat{\Phi}(r) Y_l e^{-i\sigma t} \\ \xi^r &= \eta_r(r) Y_l e^{-i\sigma t} \\ \xi^\theta &= \frac{\eta_\perp(r)}{r^2} \partial_\theta Y_l e^{-i\sigma t}. \end{split} \tag{3.9}$$

We will assume  $l \neq 0$ . The angular frequency is  $\sigma = 2\pi f$ . Note that we are using the coordinate basis  $\{(\partial_r)^i, (\partial_\theta)^i, (\partial_\phi)^i\}$  rather than the normalized coordinate basis  $\{\hat{r}, \hat{\theta}, \hat{\phi}\}$ , which explains the last Ansatz having  $\eta_\perp/r^2$  rather than  $\eta_\perp/r$ . Plugging these Ansätze into Eq. (3.7) gives us a relation to eliminate  $\delta \hat{P}$  via

$$\delta \hat{P} = \rho (\sigma^2 \eta_{\perp} - \delta \hat{\Phi}). \tag{3.10}$$

The adiabatic condition then yields a relation which can be used to eliminate  $\delta \hat{\rho}$  via

$$\delta\hat{\rho} = \rho \left( \frac{\sigma^2}{c_s^2} \eta_{\perp} - \frac{\delta\hat{\Phi}}{c_s^2} - \mathcal{B}\eta_r \right), \tag{3.11}$$

where we have defined  $\mathcal{B} \equiv \partial_r \ln \rho - (1/\Gamma_1)\partial_r \ln P$  as the Schwarzschild discriminant. In what follows, we also define  $\tilde{G} \equiv \partial_r P/\rho = -\partial_r \Phi$ , and the Brunt-Väisälä frequency squared is  $N^2 = \tilde{G}\mathcal{B}$ . The linearization of the remaining Eqs. (3.5), (3.6), and (3.8) yields

$$0 = \partial_r \eta_r + \left[ \frac{2}{r} + \frac{\partial_r P}{\Gamma_1 P} \right] \eta_r$$
$$+ \left[ \frac{\sigma^2}{c_s^2} - \frac{l(l+1)}{r^2} \right] \eta_\perp - \frac{1}{c_s^2} \delta \hat{\Phi}$$
(3.12)

$$0 = \partial_r \eta_{\perp} - \left[ 1 - \frac{N^2}{\sigma^2} \right] \eta_r + \mathcal{B} \eta_{\perp} - \frac{\mathcal{B}}{\sigma^2} \delta \hat{\Phi}$$
 (3.13)

$$0 = \partial_r \delta \hat{\Phi} - F \tag{3.14}$$

$$0 = \partial_r F + \frac{2}{r} F + 4\pi \rho \mathcal{B} \eta_r - 4\pi \rho \frac{\sigma^2}{c_s^2} \eta_\perp$$

$$+ \left[ \frac{4\pi \rho}{c_s^2} - \frac{l(l+1)}{r^2} \right] \delta \hat{\Phi}, \qquad (3.15)$$

where we defined  $F \equiv \partial_r \delta \hat{\Phi}$  to reduce the system to first order. In obtaining these equations, we used the identity  $\partial_\theta^2 Y_l + \cot\theta \partial_\theta Y_l = -l(l+1)Y_l$ . Note these perturbative equations are the same equations as in Ref. [24], Eqs. (31)–(33), after changing the definitions  $\delta \hat{\Phi} \leftrightarrow -\Phi'$ ,  $\xi_h \leftrightarrow \eta_\perp/r$ . The latter identification comes both from different definitions of  $\eta_\perp$  vs  $\xi_h$  as well as the use of different basis

vectors— $\{(\partial_r)^a, (\partial_\theta)^a, (\partial_\phi)^a\}$  in our case vs  $\{\hat{r}, \hat{\theta}, \hat{\phi}\}$  in Ref. [24].

To solve these equations, we integrate from a small nonzero radius  $r_0$  (typically dr/5, where dr is the grid resolution), where we impose regularity conditions (see Appendix A) in the form (assuming  $l \neq 0$ )

$$\eta_r = A_0 r^{l-1}, \qquad \eta_{\perp} = \frac{A_0}{l} r^l$$

$$\delta \hat{\Phi} = C_0 r^l, \qquad \partial_r \delta \hat{\Phi} = l C_0 r^{l-1}, \qquad (3.16)$$

where  $A_0$  is specified as a small number ( $10^{-5}$  in our case) which encodes the overall amplitude of the perturbation and  $C_0$  is searched for via a root-finding algorithm such that an outer boundary condition on  $\delta\hat{\Phi}$  is satisfied—see Appendix A for a detailed description. This outer boundary condition on  $\delta\hat{\Phi}$  was not imposed in Ref. [6], in which instead  $\delta\hat{\Phi}|_{r_0}=0=\partial_r\delta\hat{\Phi}|_{r_0}$  was used. This error was repeated in subsequent work, including Refs. [8,12,25], but does not affect any of the results obtained in the Cowling approximation.

We validate our current Newtonian perturbative scheme on a Newtonian polytropic star in Appendix B and demonstrate that the effect of ignoring the outer boundary condition on  $\delta\hat{\Phi}$  is large mode frequency errors for modes of low radial order.

We also demonstrate in Appendix B that our current Newtonian perturbative scheme recovers the nonradial modes of equilibrium stars evolved in a pseudo-Newtonian system using FLASH. This system has a phenomenologically modified monopole gravitational potential designed to mimic relativistic stars (Ref. [26], Case A). This demonstrates that we can solve for nonradial modes even though we do not have an equation of motion for the monopole potential. Such an equation never appears in our derivation above, because we assumed  $l \neq 0$ .

Having the consistent perturbative scheme for such pseudo-Newtonian simulations allows us to investigate how well other aspects of the approximation (the assumption of equilibrium background, zero background velocity, and spherical averaging) actually affect the mode identification.

The other outer boundary condition concerning the fluid variables is considerably more uncertain. In Ref. [6], it was taken to be  $\Delta P|_{r=R}=0$  for some outer boundary R representing the protoneutron star (PNS) surface and in Ref. [5] was taken to be  $\eta_r|_{\mathrm{shockwave}}=0$ . With the consistent perturbative equations, we can instead simply plug in the frequency observed in the simulation and see whether the resulting mode function matches the simulated velocity data well. We can also try to infer an appropriate outer boundary condition on the fluid variables in this way. Thus, we can turn the problem around and attempt to measure the appropriate boundary condition. Theoretically,

the boundary condition must account for the Rankine-Hugoniot jump conditions across the accretion shock, which in turn depend upon the state of the supersonically accreting material upstream from the shockwave (see, e.g., Refs. [27,28]).

## IV. RESULTS

We show the GW spectrum in Fig. 1, which is computed using a Bohman window with 35 ms width and averaged over times  $t \in [30, 50]$  ms. The gray shaded intervals indicate the frequency extent of the spectral filters used to extract the velocity data from the simulation. A snapshot of those data near t=40 ms is then matched with perturbative solutions, with the frequency as the free parameter in the perturbative solutions. The perturbative solutions whose mode function matches the velocity data best have frequencies of 507 and 1238 Hz, which compares well with the peaks in Fig. 1.

Our first finding is that plugging in the simulation frequency  $f \sim 515$  Hz (disregarding any outer boundary condition on the fluid variables) yields a perturbative solution that fits the simulation data well—see Fig. 2. In the top two panels, we show the 515 Hz perturbative solution (weighted by  $\rho^{1/4}$ ) for various boundary conditions on  $\delta\hat{\Phi}$ , namely, the vacuum one [Eq. (A10)] imposed at various radii as well as the in-matter one [Eq. (A12)] which does not depend on the outer boundary location. Note we plot on an arbitrary linear vertical scale. The result obtained using the vacuum boundary condition (appreviated "bc") approaches the in-matter one rapidly as the outer boundary moves out, because the density perturbation  $\delta \hat{\rho}$ becomes negligible for  $r \gtrsim 60$  km (see the bottom panel). For the rest of our results, we use the in-matter boundary condition (A12).

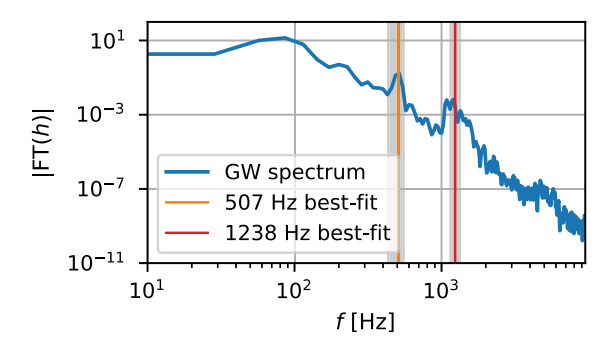


FIG. 1. Normalized GW spectrum averaged over  $t \in [30, 50]$  ms postbounce, computed using a Bohman window with 35 ms width. Two frequencies of the best fit mode functions are indicated at 507 and 1238 Hz, corresponding to weakly excited quadrupolar modes. These compare well with the peaks in the GW spectrum at 515 and 1241 Hz. The shaded areas indicate the frequency extent of the spectral filter used in Refs. [8,12] to extract the velocity data, against which perturbative mode functions are matched.

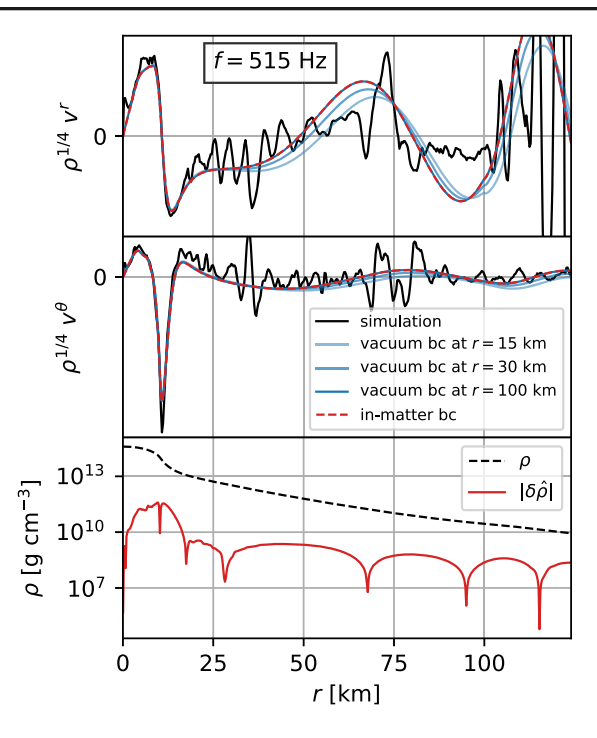


FIG. 2. Upper two panels: Normalized perturbative solutions plotted on a linear vertical scale, with frequency corresponding to the simulation, f=515 Hz, for varying outer boundary condition on the Newtonian potential perturbation. The vacuum boundary condition Eq. (A10) is imposed at  $r_{\rm bc}=\{15,30,100\}$  km, and is seen to approach the in-matter boundary condition case (A11) as the boundary is placed farther out. The perturbative solutions are a poor representation of the simulation beyond  $\sim 10$  km. Bottom panel: The density  $\rho$  and density perturbation  $|\delta\hat{\rho}|$  are displayed for reference. The density perturbation becomes negligible beyond  $\sim 60$  km. The shockwave is located at  $r \sim 125$  km at this time 40 ms post-bounce.

Next, we do a search over frequency (again disregarding outer boundary conditions for the fluid variables) to find the best-fitting perturbative solution to the simulation data. The fit quality is computed by normalizing the  $\sqrt{\rho}$ -weighted velocities and computing a Frobenius norm of their difference (see Ref. [12]). The result is shown in Fig. 3. Despite not smoothing the simulated data, the agreement is nonetheless striking. We again weight the velocity by  $\rho^{1/4}$  to allow easier visual inspection (compared to a  $\sqrt{\rho}$  weighting). We stress that this is an unforgiving way of displaying the agreement. The radial nodes of the best-fit perturbative solution are consistent with those found in Refs. [8,12], i.e., n = 4 when counted within the shockwave (which is located at  $r \sim 125$  km at this snapshot). Note that, since our background is not actually in equilibrium, we have an ambiguity in how we apply the perturbative scheme. Namely, we can set  $\tilde{G} = \partial_r P/\rho$  or  $\tilde{G} = -\partial_r \Phi^2$ . We show

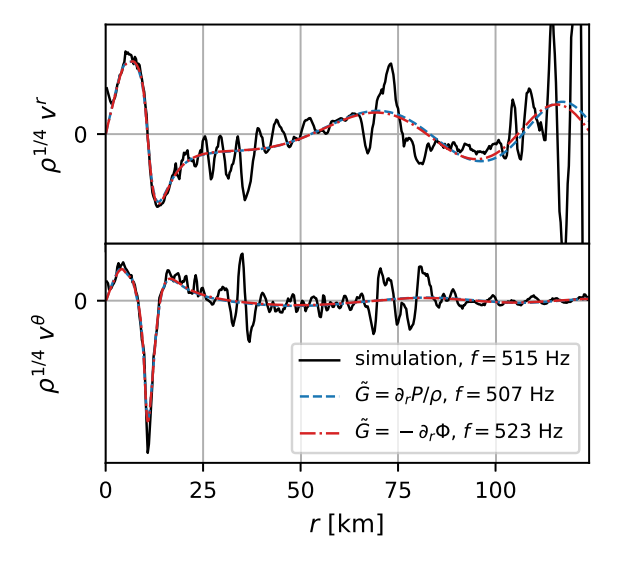


FIG. 3. The best fit perturbative solutions for two different choices  $\tilde{G} = \partial_r P/\rho$  and  $\tilde{G} = -\partial_r \Phi$ , which in a true spherically symmetric equilibrium would yield the same result. These choices yield frequencies of 507 and 523 Hz, respectively. This is a mismatch with the simulation frequency 515 Hz by  $\pm 1.6\%$ . These perturbative solutions have radial order n=4 if counted up to the shockwave location r=125 km.

both cases in Fig. 3, which yield best-fit solutions with frequencies of 507 and 523 Hz, respectively. Both choices are equally accurate for this mode, but unless otherwise specified, we will use  $\tilde{G} = \partial_r P/\rho$ .

In Fig. 4, we show the analogous plot for the 1241 Hz frequency mode, showing a similar level of agreement. The best-fitting perturbative solutions have frequencies of 1238 and 1245 Hz for the cases  $\tilde{G} = \partial_r P/\rho$  and  $\tilde{G} = -\partial_r \Phi$ , respectively. This is 0.24% and 0.32% disagreement, respectively.

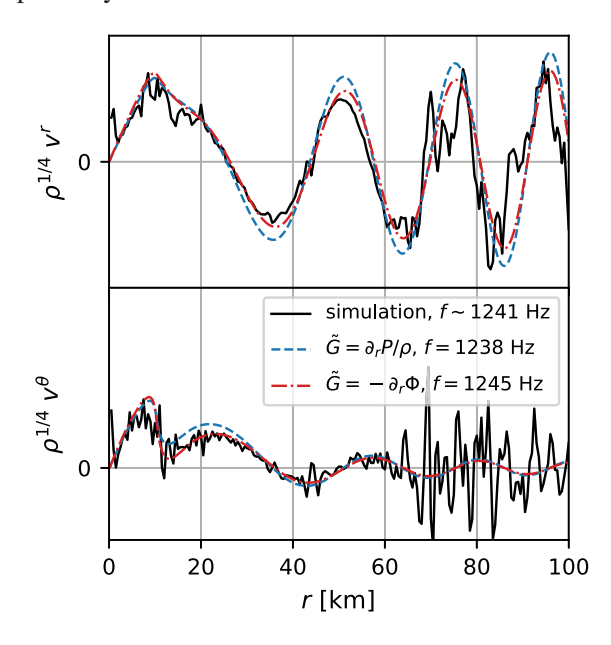


FIG. 4. Same as Fig. 3 but for the  $\sim$ 1240 Hz peak.

<sup>&</sup>lt;sup>2</sup>This is not the only ambiguity. Wherever a pressure gradient or gravitational potential gradient appears, one could switch it out with the other using  $\partial_r P = -\rho \partial_r \Phi$ .

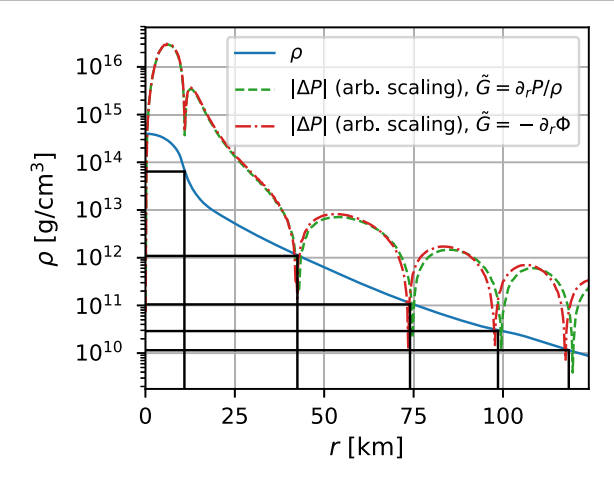


FIG. 5. Lagrangian pressure perturbation  $|\Delta P|$  corresponding to the best fit perturbative solutions in Fig. 3 displayed on an arbitrary (arb.) logarithmic scale. The rest mass density of the spherically averaged background is also displayed on an accurate logarithmic scale. Zeros of the Lagrangian pressure perturbation are indicated, which suggest appropriate values of  $\rho$  at which  $\Delta P=0$  should be enforced during a mode search.

We now reinstate outer boundary conditions for the fluid variables. Our purpose is to "measure" the boundary conditions which will yield a mode function spectrum such that the best-fit mode function has a frequency which is (at least similar to) the simulation. If such a boundary condition existed, then one could safely identify modes in pseudo-Newtonian simulations by doing frequency matching alone, removing the need for the complicated and expensive mode function matching procedure described in Refs. [8,12].

In Fig. 5, we plot the absolute value of the Lagrangian pressure perturbation corresponding to the best-fitting perturbative solutions for the 515 Hz mode in Fig. 3 on an arbitrary logarithmic scale. The analogous plot for the 1241 Hz mode is displayed in Fig. 6. The Lagrangian pressure perturbation is overlaid on the background density

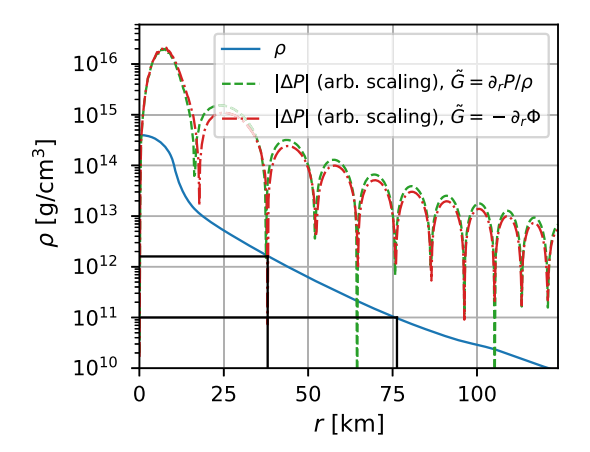


FIG. 6. Same as Fig. 5 but for the ~1240 Hz mode. The zeros of  $\Delta P$  occurring near  $\rho = 10^{12}$ ,  $10^{11}$  g cm<sup>-3</sup> are shown.

TABLE I. Modes with nearest  $(f_{\text{best}})$  and next-nearest  $(f_{\text{next}})$  frequencies to the simulation value of 515 Hz, for varying boundary conditions. We use  $\tilde{G} = \partial_r P/\rho$ . The subscripts on  $\Delta P$  (eg.  $\Delta P|_{\rho \sim 10^{12}}$ ) indicate density in units of g cm<sup>-3</sup>. The nearest modes are highlighted in bold.

Boundary condition	$f_{\mathrm{best}}$ (Hz), diff	$n_{ m best}$	$f_{\text{next}}$ (Hz), diff	$n_{\text{next}}$
$\Delta P _{\rho \sim 10^{12}} = 0$	504, -2.1%	4	381, -26%	4
$\begin{array}{l} \Delta P _{\rho \sim 10^{12}} = 0 \\ \Delta P _{\rho \sim 10^{11}} = 0 \\ \Delta P _{\rho \sim 10^{10}} = 0 \end{array}$	504, -2.1%	4	436, -15%	5
$\Delta P _{\rho \sim 10^{10}} = 0$	503, -2.3%	4	463, -10%	5
$ \eta_r _{\text{shockwave}} = 0$	513, -0.4%	4	491, -4.7%	5

TABLE II. Same as Table I but for the  $\sim$ 1240 Hz mode. Nodes are counted up to the shockwave at r = 125 km.

Boundary condition	$f_{\mathrm{best}}$ (Hz), diff	$n_{ m best}$	$f_{\text{next}}$ (Hz), diff	$n_{\text{next}}$
$\Delta P _{a \sim 10^{12}} = 0$	1101, -11%	8	1532, +23%	12
$\Delta P _{\rho \sim 10^{12}} = 0$ $\Delta P _{\rho \sim 10^{11}} = 0$ $\Delta P _{\rho \sim 10^{10}} = 0$	1239, -0.2%	9	1073, -14%	8
$\Delta P _{\rho \sim 10^{10}} = 0$	1235, -0.5%	9	1357, +9.3%	10
$ \eta_r _{\text{shockwave}} = 0$	1248, -0.6%	9	1137, -8.4%	8

profile, which is plotted on a faithful logarithmic scale. We indicate the location of the zero crossings of  $\Delta P$  with dotted lines and also indicate the corresponding density value there. Zero crossings for the 515 Hz case occur near  $\{6\times10^{13},10^{12},10^{11},10^{10}\}\ \mathrm{g\,cm^{-3}}$ . A common definition for the PNS surface is, e.g.,  $\rho=10^{11}\ \mathrm{g\,cm^{-3}}$ , and a zero crossing at that location also occurs for the 1241 Hz mode in Fig. 6. These zero crossings are not enforced, and if they are not mere coincidences, then they could be physically meaningful if they work for different modes.

In Tables I and II, for various outer boundary conditions on the fluid variables, we show the mode properties with nearest and next-nearest frequencies to the simulation (subscripts best and next, respectively). All choices listed, aside from  $\Delta P|_{\rho=10^{12}}=0$ , which fails to reproduce the 1241 Hz mode, yield a clear relative distinction between the best-fit and the next-best one and could therefore be regarded as safe to use during a mode frequency matching procedure. However, the boundary condition of Ref. [5],  $\eta_r|_{\text{shockwave}}=0$ , yields remarkable sub-1% agreement for both modes, suggesting it is the physically correct one in this regime.

### V. CONCLUSIONS

In this work, we presented and tested perturbative equations, which are the consistent linear approximation of pseudo-Newtonian systems whereby one uses Newtonian hydrodynamics, standard Newtonian gravity for nonradial components of the potential, and some nonstandard monopole potential such as that of Ref. [26], Case A. This system of

equations allows one to solve for nonradial modes, thereby allowing identification of active modes in pseudo-Newtonian simulations (e.g., PROMETHEUS/VERTEX [2,14–17], [18,19], FORNAX [20], and CHIMERA [21]) using mode frequency matching. This alleviates the need to perform the complex and expensive mode function matching procedure of Refs. [8,12].

We found that the imposing vanishing radial displacement as an outer boundary condition (as in Ref. [5]) yields remarkable sub-1% agreement between perturbative mode frequencies and the simulation, suggesting that this is the physically correct choice. However, imposing a vanishing Lagrangian pressure perturbation at the radii where  $\rho = \{10^{11}, 10^{10}\}$  g cm<sup>-3</sup> (the last value being used in Ref. [6]) should also prevent mode misidentification. These conclusions ought to be tested in other regimes, e.g., later times t > 100 ms and different progenitor stars.

#### ACKNOWLEDGMENTS

We thank Evan O'Connor for comments and insight regarding neutrino pressure gradients and both Evan O'Connor and Sean M. Couch for FLASH code development and running the simulations analyzed in this work. We also thank an anonymous referee for providing a deeper context of this work within the existing literature. This research was supported by National Science Foundation Grant No. PHY-1912619 at the University of Arizona. Software used was MATPLOTLIB [29], FLASH [18,19,30,31], and SciPy [32].

### APPENDIX A: BOUNDARY CONDITIONS

In this Appendix, we give details of how boundary conditions are derived, for the purpose of being pedagogical. We use the strategy of Ref. [33], except applied directly to our Eqs. (3.12)–(3.15).

We wish to determine the behavior of  $\{\eta_r, \eta_\perp, \delta \hat{\Phi}\}$  in a neighborhood of the origin r = 0. For this purpose, we make the Ansatz

$$\eta_r = r^a \sum_{n=0}^{\infty} A_n r^n$$
 $\eta_{\perp} = r^b \sum_{n=0}^{\infty} B_n r^n$ 
 $\delta \hat{\Phi} = r^c \sum_{n=0}^{\infty} C_n r^n$ ,

where  $A_n$ ,  $B_n$ ,  $C_n$  are constant coefficients nonzero when n=0 (do not confuse n in this context with the radial order of modes) and a, b, c are constant exponents to be determined. We require a, b,  $c \ge 0$  by regularity at the origin. This Ansatz is a generalization of the Frobenius method to a system of equations. The derivatives we need are

$$\partial_r \delta \hat{\Phi} = r^c \sum_{n=0}^{\infty} (n+c) C_n r^{n-1}$$
 (A1)

$$\partial_r^2 \delta \hat{\Phi} = r^c \sum_{n=0}^{\infty} (n+c)(n+c-1)C_n r^{n-2} \qquad (A2)$$

and similar expressions for  $\partial_r \eta_r$ ,  $\partial_r \eta_{\perp}$ .

 $Q_a = \sum_{n=0}^{\infty} nA_n r^{n-1} + \left[ \frac{2+a}{r} + \frac{\partial_r P}{\Gamma_1 P} \right] \sum_{n=0}^{\infty} A_n r^n$ 

Plugging these Ansätze into our Eqs. (3.12)–(3.15) and collecting terms proportional to  $r^a$ ,  $r^b$ ,  $r^c$ , we schematically obtain

$$0 = Q_{a}r^{a} + Q_{b}r^{b} + Q_{c}r^{c}$$

$$0 = R_{a}r^{a} + R_{b}r^{b} + R_{c}r^{c}$$

$$0 = S_{a}r^{a} + S_{b}r^{b} + S_{c}r^{c},$$
(A3)

where the coefficients are

$$Q_{b} = \left[\frac{\sigma^{2}}{c_{s}^{2}} - \frac{l(l+1)}{r^{2}}\right] \sum_{n=0}^{\infty} B_{n} r^{n}$$

$$Q_{c} = -\frac{1}{c_{s}^{2}} \sum_{n=0}^{\infty} C_{n} r^{n}$$

$$R_{a} = -\left[1 - \frac{N^{2}}{\sigma^{2}}\right] \sum_{n=0}^{\infty} A_{n} r^{n}$$

$$R_{b} = \sum_{n=0}^{\infty} n B_{n} r^{n-1} + \left[\frac{b}{r} + \mathcal{B}\right] \sum_{n=0}^{\infty} B_{n} r^{n}$$

$$R_{c} = -\frac{\mathcal{B}}{\sigma^{2}} \sum_{n=0}^{\infty} C_{n} r^{n}$$

$$S_{a} = 4\pi \rho \mathcal{B} \sum_{n=0}^{\infty} A_{n} r^{n}$$

$$S_{b} = -4\pi \rho \frac{\sigma^{2}}{c_{s}^{2}} \sum_{n=0}^{\infty} B_{n} r^{n}$$

$$S_{c} = \sum_{n=0}^{\infty} n^{2} C_{n} r^{n-2} + \left[\frac{2c+1}{r}\right] \sum_{n=0}^{\infty} n C_{n} r^{n-1}$$

$$+ \left[\frac{c(c+1) - l(l+1)}{r^{2}} + \frac{4\pi \rho}{c_{s}^{2}}\right] \sum_{n=0}^{\infty} C_{n} r^{n}. \tag{A4}$$

Since Eqs. (A4) hold in a neighborhood of the origin, the full coefficients in front of each power of r (once collected) must vanish independently. We are interested in the vanishing of the lowest-order terms.

In the Frobenius method, only one equation is being solved. This means only one unknown exponent (e.g., a above) appears in the equation once the Ansatz is plugged in. This makes identifying orders in r straightforward.

In our case, we have a system of equations, and multiple unknown exponents a, b, c appear in each equation. This makes identifying orders in r more complicated, but we can proceed by considering all possible cases and systematically eliminating them. This is what we do next.

Since we are interested in the lowest nontrivial order, it suffices to truncate every sum after the first nonzero term. We also need to consider the order carried by the background quantities. In particular, since the pressure and density are spherically symmetric quantities with even parity, we have  $P \simeq P|_0 + P''r^2/2$  and  $\rho \simeq \rho|_0 + \rho''r^2/2$ , where we use a double prime superscript to denote a second radial derivative evaluated at the origin, to avoid cumbersome notation. This means  $\partial_r P = P''r = \mathcal{O}(r)$  and  $\partial_r \rho = \rho''r = \mathcal{O}(r)$ . Thus,  $\mathcal{B} = \partial_r \rho/\rho - \partial_r P/(\Gamma_1 P) \simeq [\rho''/\rho - P''/(\Gamma_1 P)]r = \mathcal{O}(r)$ . Similarly,  $\tilde{G} = \partial_r P/\rho \simeq P''r/\rho = \mathcal{O}(r)$ , and so by extension,  $N^2 = \tilde{G}\mathcal{B} = \mathcal{O}(r^2)$ . Inserting these expansions into Eqs. (A4) and keeping lowest-order terms for each of the  $r^a$ ,  $r^b$ ,  $r^c$  terms separately, we obtain

$$0 = (2+a)A_0r^{a-1} - B_0l(l+1)r^{b-2} - \frac{C_0}{c_s^2}r^c$$
 (A5)

$$0 = -A_0 r^a + B_0 b r^{b-1} - \frac{C_0}{c_s^2} \left[ \frac{\rho''}{\rho} - \frac{P''}{\Gamma_r P} \right] r^{c+1}$$
 (A6)

$$0 = 4\pi\rho \left[ \frac{\rho \prime \prime}{\rho} - \frac{P \prime \prime}{\Gamma_1 P} \right] A_0 r^{a+1} - 4\pi\rho \frac{\sigma^2}{c_s^2} B_0 r^b + [c(c+1) - l(l+1)] C_0 r^{c-2}. \tag{A7}$$

At this stage, we do not know whether we have kept consistent orders in r, since we do not know the relationship between the exponents a, b, c. However, when considering Eq. (A7), notice that the exponents will not depend upon the background solution if and only if the  $r^{c-2}$  term is the lowest-order one. Independence from the background solution is a property we desire<sup>3</sup>; thus, we demand that the  $r^{c-2}$  term must vanish, i.e., c = l. This also implies c - 2 < a + 1 and c - 2 < b.

The same consideration applied to Eq. (A5) means that one or both of the  $r^{a-1}$  and  $r^{b-2}$  terms must be lowest order. If the  $r^{b-2}$  term is lowest order by itself, that implies l=0. If we are not interested in radial modes (in this work, we are not), then we can discard this possibility. On the other hand, if the  $r^{a-1}$  term is lowest order by itself, that implies a=-2, which would violate regularity at the origin. Thus, we must conclude that both terms are lowest order, i.e., a=b-1 and  $(2+a)A_0=B_0l(l+1)$ .

Lastly, consider Eq. (A6). If the exponents are to be independent of the background quantities, then one or both

of the  $r^a$  and  $r^{b-1}$  terms must be lowest order. But we already established that a=b-1; thus, they are both lowest order. This yields  $A_0=bB_0$ . Combining this relation with the one obtained previously from Eq. (A5) and using a=b-1, we finally find

$$a = l - 1,$$
  $b = l,$   $c = l.$  (A8)

Therefore, in a neighborhood of the origin,

$$\eta_r = A_0 r^{l-1}, \qquad \eta_\perp = \frac{A_0}{l} r^l$$

$$\delta \hat{\Phi} = C_0 r^l, \qquad \partial_r \delta \hat{\Phi} = l C_0 r^{l-1}. \tag{A9}$$

Beware that we are not using the normalized coordinate basis. In the normalized basis, one instead has  $\eta_{\perp} = (A_0/l)r^{l-1}$ .

In the numerical integration, we begin a small distance away from the origin (e.g., dr/5, where dr is the grid resolution) and use Eqs. (A9) as initial conditions. This requires specification of  $A_0$ ,  $C_0$  and the angular frequency  $\sigma$ . The choice of  $A_0$  amounts to an arbitrary amplitude, which we choose to be  $A_0 = 10^{-5}$ .

For each value of angular frequency  $\sigma$ , we perform a root-finding procedure to converge upon the value of  $C_0$  such that at the outer boundary r = R we have [24]

$$\left[ \partial_r \delta \hat{\Phi} + \frac{l+1}{r} \delta \hat{\Phi} \right]_{r=R} = 0.$$
 (A10)

This relation can be derived from the solution for the *l*th spherical harmonic moment of the Poisson equation [23]

$$\delta\hat{\Phi} = -\frac{4\pi}{2l+1} \frac{1}{R^{l+1}} \int_0^r \delta\hat{\rho}(\tilde{r}) \tilde{r}^{l+2} d\tilde{r}, \qquad (A11)$$

valid when  $\delta \hat{\rho}(r) = 0$  for r > R. In the case of our CCSN system, lth moment rest mass perturbations  $\delta \hat{\rho}$  likely escape out through r = R, but to the extent that it is of small amplitude and leaks into different harmonics  $l' \neq l$ , it can be ignored. If it cannot be ignored, then one should instead integrate the perturbative system beyond r = R and then impose

$$\left[ \partial_r \delta \hat{\Phi} + \frac{l+1}{r} \delta \hat{\Phi} \right]_{r=R} = -4\pi R^{l-1} \int_R^{\infty} \frac{\delta \hat{\rho}}{r^{l-1}} dr, \quad (A12)$$

where the infinite upper limit of integration is understood to be replaced by an appropriate outermost radius, e.g., the grid boundary or the CCSN shockwave. When using Eq. (A12), one must integrate past R in order to obtain  $\delta \hat{\rho}$  over the domain of interest. The choice of R is irrelevant. Note that

<sup>&</sup>lt;sup>3</sup>Although it would be interesting to know whether "special" perturbations of stars with exponents depending upon the background solution are ever relevant in practice.

$$\delta\hat{\rho} = \rho \left( \frac{\sigma^2}{c_s^2} \eta_{\perp} - \frac{\delta\hat{\Phi}}{c_s^2} - \mathcal{B}\eta_r \right). \tag{A13}$$

Also, it is advisable to enforce Eq. (A10) at the outer boundary rather than Eq. (A11), in order to get control of the first derivative  $\partial_r \delta \hat{\Phi}$ .

The root-finding loop for  $C_0$  is nested inside a root finder for the angular frequency  $\sigma$ , which yields either vanishing Lagrangian pressure perturbation at the outer boundary

$$\Delta P|_{R} = [\rho \sigma^{2} \eta_{\perp} - \rho \delta \hat{\Phi} + \eta_{r} \partial_{r} P]|_{R} = 0, \quad (A14)$$

corresponding to a free surface, or vanishing radial displacement

$$\eta_r|_R = 0, \tag{A15}$$

depending on one's choice.

## APPENDIX B: TESTS OF PERTURBATIVE SCHEME

In this section, we demonstrate the accuracy of our mode solver on both a Newtonian polytropic star and a pseudo-Newtonian "Tolman-Oppenheimer-Volkoff" star.

## 1. Newtonian polytropic star

Figure 7 displays a comparison between l=1 and l=2 mode frequencies we obtain for a  $\Gamma=5/3$  Newtonian polytropic star. The polytropic constant  $\kappa$ , where  $P=\kappa\rho^{\Gamma}$ , is arbitrary, and we display the frequencies in dimensionless form

$$\omega \equiv \sqrt{\frac{\sigma^2}{4\pi G \rho_c}},\tag{B1}$$

where  $\sigma=2\pi f$  is the angular frequency and  $\rho_c$  is the central rest mass density. We impose a vanishing Lagrangian pressure perturbation at the surface, Eq. (A14). We terminate the frequency search when the update becomes smaller than 0.5 Hz (we set the stellar mass to  $M=1.4~M_{\odot}$  and radius to  $R=12~{\rm km}$ , yielding mode frequencies roughly greater than or equal to 2 kHz. The frequencies compare favorably with past work (Ref. [34], p. 387, and references therein), except when the outer boundary condition for the Newtonian potential is disregarded (setting  $\delta \hat{\Phi} = \partial_r \delta \hat{\Phi} = 0$  at the starting point of outward integration), as done in Ref. [6] and repeated in subsequent work, including Refs. [8,12,25].

#### 2. FLASH Tolman-Oppenheimer-Volkoff star

Figure 8 displays a comparison between l=2 modes computed perturbatively in this work with those extracted in Refs. [8,12] from a fully nonlinear FLASH simulation of an equilibrium  $\Gamma=2$  star with  $\kappa=100$  and  $\rho_c=1.28\times 10^{-3}$  in geometrized units. We impose vanishing Lagrangian

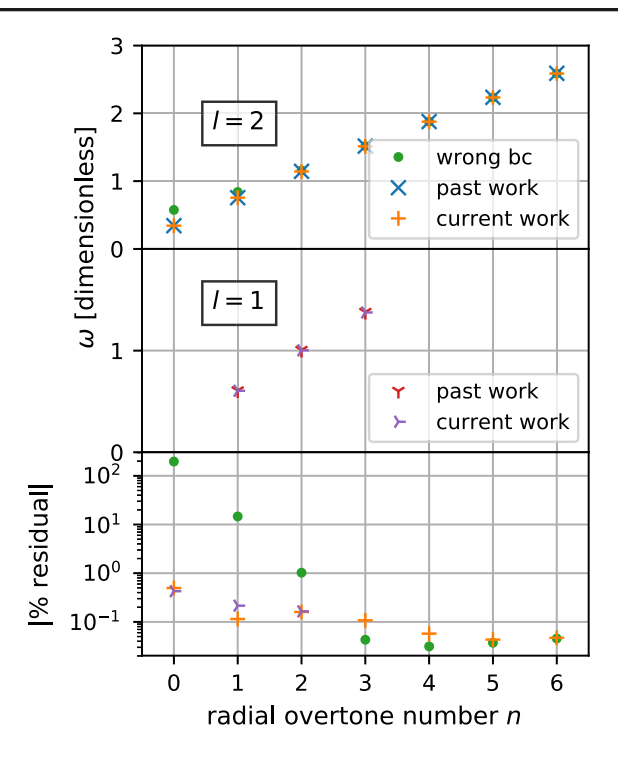


FIG. 7. Comparison between axisymmetric l=1 and l=2 mode frequencies obtained in this work vs past work (Ref. [34], p. 387) for a  $\Gamma=5/3$  polytrope. The frequencies are displayed in dimensionless form  $\omega=\sqrt{\sigma^2/4\pi G\rho_c}$ , where  $\sigma=2\pi f$  is the angular frequency and  $\rho_c$  is the central density. The wrong boundary condition  $\delta\hat{\Phi}|_{r_0}=0=\partial_r\delta\hat{\Phi}|_{r_0}$  (green dots) has a large error for the lower overtones. With the correct boundary conditions [Eqs. (A9)], we obtain at worst  $\sim 0.4\%$  residual for the fundamental n=0 mode.

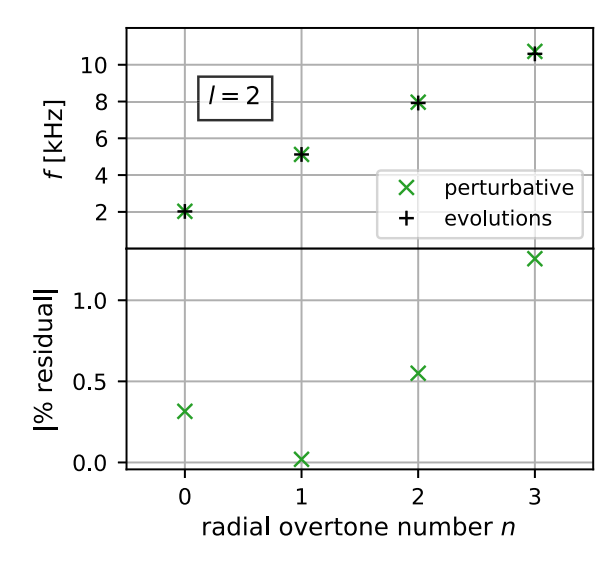


FIG. 8. Comparison between axisymmetric l=2 mode frequencies obtained perturbatively in this work vs using full nonlinear FLASH evolutions in past work [8,12], for a  $\Gamma=2$  polytropic star with  $P=\kappa\rho^{\Gamma}$ ,  $\rho_c=1.28\times 10^{-3}$ , and  $\kappa=100$  in geometrized units.

pressure perturbation at the surface, Eq. (A14). The frequency search terminates when the update is less than 0.5 Hz.

This test demonstrates that the nonradial modes of pseudo-Newtonian systems, as simulated in, e.g., FLASH [18,19], FORNAX [20], and CHIMERA [21], are determined by a purely Newtonian perturbative calculation. Radial perturbations of the gravitational potential, which would require knowledge of an equation of motion determining the "effectively GR" monopole (Ref. [26], Case A), do not arise anywhere when one solves for nonradial modes.

## 3. CCSN system

We know based on the previous tests that the perturbative system is the consistent linearization of the equations of motion being simulated. However, when applying it to the CCSN system, we are dealing with a nonspherical system, which we subject to a spherical averaging before performing the perturbative calculation, and it is not in hydrostatic equilibrium. In Fig. 9, we compare the magnitude of different terms in the spherically symmetric Euler equation

$$0 = \partial_t(\rho v^r) + \frac{1}{r^2} \partial_r(r^2 \rho v^r v^r) + \partial_r P + \rho \partial_r \Phi, \quad (B2)$$

as a percentage comparison to  $|\partial_r P|$ . The equilibrium condition  $\partial_r P + \rho \partial_r \Phi$  is satisfied at the ~5% level. Note that neutrino pressure gradients should also have a contribution to this balance, but their perturbations would introduce additional equations of motion, so we have decided to neglect them. Furthermore, neutrino pressure gradients should gradually decouple from the fluid as one moves away from the PNS center, so introducing them into the background solution requires care. The level of

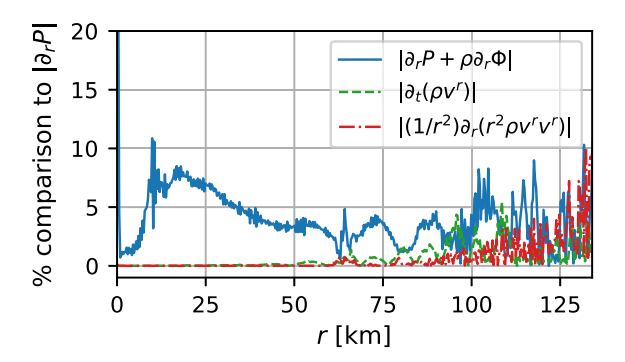


FIG. 9. A comparison between the magnitude of different terms in the spherically symmetric Euler equation, as applied to the spherically averaged snapshot of the CCSN system at 40 ms. The equilibrium condition  $\partial_r P + \rho \partial_r \Phi = 0$  is only satisfied at the ~5% level, which is commensurate with the frequency mismatch between the simulation and the best fit perturbative solution. The nonequilibrium terms  $\partial_t (\rho v^r)$  and  $r^{-2} \partial_r (\rho v^r v^r)$  give a negligible contribution to the balance at r < 50 km (sub-0.1%), and rises to ~1% around r = 100 km.

violation of the hydrostatic equilibrium condition should be taken as a cautionary note when applying this perturbative calculation to dynamical systems such as CCSNe.

By comparison, the other terms which encode time dependence of the background solution  $[\partial_t(\rho v^r)]$  or its nonsteadiness  $(v^r = \text{constant} \neq 0)$  are not large enough to account for the degree of nonequilibrium (sub-0.1% for r < 50 km rising to 1% around r = 100 km). This suggests that generalizing the perturbative scheme to a time-dependent or unsteady background would not yield significant improvements in the perturbative calculations presented in this work.

J. W. Murphy, C. D. Ott, and A. Burrows, Astrophys. J. 707, 1173 (2009).

<sup>[2]</sup> B. Müller, H.-T. Janka, and A. Marek, Astrophys. J. 766, 43 (2013).

<sup>[3]</sup> P. Cerdá-Durán, N. DeBrye, M. A. Aloy, J. A. Font, and M. Obergaulinger, Astrophys. J. Lett. **779**, L18 (2013).

<sup>[4]</sup> J. Fuller, H. Klion, E. Abdikamalov, and C. D. Ott, Mon. Not. R. Astron. Soc. 450, 414 (2015).

<sup>[5]</sup> A. Torres-Forné, P. Cerdá-Durán, A. Passamonti, and J. A. Font, Mon. Not. R. Astron. Soc. 474, 5272 (2018).

<sup>[6]</sup> V. Morozova, D. Radice, A. Burrows, and D. Vartanyan, Astrophys. J. 861, 10 (2018).

<sup>[7]</sup> A. Torres-Forné, P. Cerdá-Durán, A. Passamonti, M. Obergaulinger, and J. A. Font, Mon. Not. R. Astron. Soc. 482, 3967 (2019).

<sup>[8]</sup> J. R. Westernacher-Schneider, Turbulence, gravity, and multimessenger asteroseismology, Ph.D. thesis, University of Guelph, located in Ontario, Canada, 2018.

<sup>[9]</sup> A. Torres-Forné, P. Cerdá-Durán, M. Obergaulinger, B. Muller, and J. A. Font, Phys. Rev. Lett. **123**, 051102 (2019).

<sup>[10]</sup> D. Vartanyan, A. Burrows, and D. Radice, Mon. Not. R. Astron. Soc. 489, 2227 (2019).

<sup>[11]</sup> H. Sotani, T. Kuroda, T. Takiwaki, and K. Kotake, Phys. Rev. D 99, 123024 (2019).

<sup>[12]</sup> J. R. Westernacher-Schneider, E. O'Connor, E. O'Sullivan, I. Tamborra, M.-R. Wu, S. M. Couch, and F. Malmenbeck, Phys. Rev. D 100, 123009 (2019).

<sup>[13]</sup> M. L. Warren, S. M. Couch, E. P. O'Connor, and V. Morozova, arXiv:1912.03328.

<sup>[14]</sup> M. Rampp and H.-T. Janka, Astron. Astrophys. 396, 361 (2002).

<sup>[15]</sup> B. Müller, H.-T. Janka, and H. Dimmelmeier, Astrophys. J. Suppl. Ser. 189, 104 (2010).

<sup>[16]</sup> B. Müller, H.-T. Janka, and A. Marek, Astrophys. J. 756, 84 (2012).

<sup>[17]</sup> B. Müller and H.-T. Janka, Astrophys. J. 788, 82 (2014).

- [18] B. Fryxell, K. Olson, P. Ricker, F. Timmes, M. Zingale, D. Lamb, P. MacNeice, R. Rosner, J. Truran, and H. Tufo, Astrophys. J. Suppl. Ser. 131, 273 (2000).
- [19] A. Dubey, K. Antypas, M. K. Ganapathy, L. B. Reid, K. Riley, D. Sheeler, A. Siegel, and K. Weide, Parallel Comput. 35, 512 (2009).
- [20] M. A. Skinner, J. C. Dolence, A. Burrows, D. Radice, and D. Vartanyan, Astrophys. J. Suppl. Ser. 241, 7 (2019).
- [21] S. W. Bruenn, J. M. Blondin, W. R. Hix, E. J. Lentz, O. Messer, A. Mezzacappa, E. Endeve, J. A. Harris, P. Marronetti, R. D. Budiardja *et al.*, arXiv:1809.05608.
- [22] B. Mueller, H. Dimmelmeier, and E. Mueller, Astron. Astrophys. 489, 301 (2008).
- [23] E. Poisson and C. M. Will, *Gravity: Newtonian, Post-Newtonian, Relativistic* (Cambridge University Press, Cambridge, England, 2014).
- [24] J. Christensen-Dalsgaard, G. Berthomieu, A. Cox, W. Livingston, and M. Matthews, *Solar Interior and Atmos*phere (University of Arizona, Tucson, 1991).

- [25] D. Radice, V. Morozova, A. Burrows, D. Vartanyan, and H. Nagakura, Astrophys. J. Lett. 876, L9 (2019).
- [26] A. Marek, H. Dimmelmeier, H.-T. Janka, E. Müller, and R. Buras, Astron. Astrophys. **445**, 273 (2006).
- [27] T. Foglizzo, P. Galletti, L. Scheck, and H.-T. Janka, Astrophys. J. **654**, 1006 (2007).
- [28] J. M. Laming, Astrophys. J. 659, 1449 (2007).
- [29] J. D. Hunter, Comput. Sci. Eng. 9, 90 (2007).
- [30] S. M. Couch, Astrophys. J. **765**, 29 (2013).
- [31] E. P. O'Connor and S. M. Couch, Astrophys. J. **854**, 63 (2018).
- [32] E. Jones, T. Oliphant, P. Peterson et al., SciPy: Open source scientific tools for PYTHON (2001), https://www .scienceopen.com/document?vid=ab12905a-8a5b-43d8-a2bbdefc771410b9.
- [33] M. Hurley, P. Roberts, and K. Wright, Astrophys. J. 143, 535 (1966).
- [34] G. P. Horedt, *Polytropes: Applications in Astrophysics and Related Fields* (Springer Science & Business Media, New York, 2004), Vol. 306.